28. Dark Energy

Revised August 2019 by D.H. Weinberg (Ohio State U.) and M. White (UC Berkeley; LBNL).

28.1 Repulsive Gravity and Cosmic Acceleration

In the first modern cosmological model, Einstein [1] modified his field equation of General Relativity (GR), introducing a "cosmological term" that enabled a solution with time-independent, spatially homogeneous matter density $\rho_{\rm m}$ and constant positive space curvature. Although Einstein did not frame it this way, one can view the "cosmological constant" Λ as representing a constant energy density of the vacuum [2], whose repulsive gravitational effect balances the attractive gravity of matter and thereby allows a static solution. After the development of dynamic cosmological models [3,4] and the discovery of cosmic expansion [5], the cosmological term appeared unnecessary, and Einstein and de Sitter [6] advocated adopting an expanding, homogeneous and isotropic, spatially flat, matter-dominated Universe as the default cosmology until observations dictated otherwise. Such a model has matter density equal to the critical density, $\Omega_{\rm m} \equiv \rho_{\rm m}/\rho_{\rm c} = 1$, and negligible contribution from other energy components [7].

By the mid-1990s, the Einstein-de Sitter model was showing numerous cracks, under the combined onslaught of data from the cosmic microwave background (CMB), large-scale galaxy clustering, and direct estimates of the matter density, the expansion rate (H_0), and the age of the Universe. As noted in a number of papers from this time, introducing a cosmological constant offered a potential resolution of many of these tensions, yielding the most empirically successful version of the inflationary cold dark matter scenario. In the late 1990s, supernova surveys by two independent teams provided direct evidence for accelerating cosmic expansion [8, 9], establishing the cosmological constant model (with $\Omega_{\rm m} \simeq 0.3$, $\Omega_\Lambda \simeq 0.7$) as the preferred alternative to the $\Omega_{\rm m} = 1$ scenario. Shortly thereafter, CMB evidence for a spatially flat Universe [10, 11], and thus for $\Omega_{\rm tot} \simeq 1$, cemented the case for cosmic acceleration by firmly eliminating the free-expansion alternative with $\Omega_{\rm m} \ll 1$ and $\Omega_\Lambda = 0$. Today, the accelerating Universe is well established by multiple lines of independent evidence from a tight web of precise cosmological measurements.

As discussed in the Big Bang Cosmology article of this *Review* (Sec. 22), the scale factor $R(t)$ of a homogeneous and isotropic Universe governed by GR grows at an accelerating rate if the pressure $p < -\frac{1}{3}\rho$ (in $c = 1$ units). A cosmological constant has $\rho_\Lambda =$ constant and pressure $p_\Lambda = -\rho_\Lambda$ (see Eq. 22.10), so it will drive acceleration if it dominates the total energy density. However, acceleration could arise from a more general form of "dark energy" that has negative pressure, typically specified in terms of the equation-of-state-parameter $w = p/\rho$ ($= -1$ for a cosmological constant). Furthermore, the conclusion that acceleration requires a new energy component beyond matter and radiation relies on the assumption that GR is the correct description of gravity on cosmological scales. The title of this article follows the common but inexact usage of "dark energy" as a catch-all term for the origin of cosmic acceleration, regardless of whether it arises from a new form of energy or a modification of GR. Our account here draws on the much longer review of cosmic acceleration by Ref. [12], which provides background explanation and extensive literature references for the discussion in Secs. 28.2 and 28.3.

Below we will use the abbreviation ΛCDM to refer to a model with cold dark matter, a cosmological constant, inflationary initial conditions, standard radiation and neutrino content, and a flat Universe with $\Omega_{\rm tot} = 1$ (though we will sometimes describe this model as "flat ΛCDM" to emphasize this last restriction). We will use wCDM to denote a model with the same assumptions but a free, constant value of w. Models with the prefix "o" (*e.g.*, `owCDM`) allow non-zero space curvature.

28.2 Theories of Cosmic Acceleration

28.2.1 *Dark Energy or Modified Gravity?*

A cosmological constant is the mathematically simplest, and perhaps the physically simplest, theoretical explanation for the accelerating Universe. The problem is explaining its unnaturally small magnitude, as discussed in Sec. 22.4.7of this *Review*. An alternative (which still requires finding a way to make the cosmological constant zero or at least negligibly small) is that the accelerating cosmic expansion is driven by a new form of energy such as a scalar field [13] with potential $V(\phi)$. The energy density and pressure of the field $\phi(\mathbf{x})$ take the same forms as for inflationary scalar fields, given in Eq. (22.52) of the Big Bang Cosmology article. In the limit that $\frac{1}{2}\dot{\phi}^2 \ll |V(\phi)|$, the scalar field acts like a cosmological constant, with $p_\phi \simeq -\rho_\phi$. In this scenario, today's cosmic acceleration is closely akin to the epoch of inflation, but with radically different energy and timescale.

More generally, the value of $w = p_\phi/\rho_\phi$ in scalar field models evolves with time in a way that depends on $V(\phi)$ and on the initial conditions $(\phi_i, \dot{\phi}_i)$; some forms of $V(\phi)$ have attractor solutions in which the late-time behavior is insensitive to initial values. Many forms of time evolution are possible, including ones where w is approximately constant and broad classes where w "freezes" towards or "thaws" away from $w = -1$, with the transition occurring when the field comes to dominate the total energy budget. If ρ_ϕ is even approximately constant, then it becomes dynamically insignificant at high redshift, because the matter density scales as $\rho_\mathrm{m} \propto (1+z)^3$. "Early dark energy" models are ones in which ρ_ϕ is a small but not negligible fraction (*e.g.*, a few percent) of the total energy throughout the matter- and radiation-dominated eras, tracking the dominant component before itself coming to dominate at low redshift.

Instead of introducing a new energy component, one can attempt to modify gravity in a way that leads to accelerated expansion [14]. One option is to replace the Ricci scalar $\mathcal{R}$ with a function $\mathcal{R} + f(\mathcal{R})$ in the gravitational action [15]. Other changes can be more radical, such as introducing extra dimensions and allowing gravitons to "leak" off the brane that represents the observable Universe (the "DGP" model [16]). The DGP example has inspired a more general class of "galileon" and massive gravity models. Constructing viable modified gravity models is challenging, in part because it is easy to introduce theoretical inconsistencies (such as "ghost" fields with negative kinetic energy), but above all because GR is a theory with many high-precision empirical successes on solar system scales [17]. Modified gravity models typically invoke screening mechanisms that force model predictions to approach those of GR in regions of high density or strong gravitational potential. Screening offers potentially distinctive signatures, as the strength of gravity (*i.e.*, the effective value of G_N) can vary by order unity in environments with different gravitational potentials.

More generally, one can search for signatures of modified gravity by comparing the history of cosmic structure growth to the history of cosmic expansion. Within GR, these two are linked by a consistency relation, as described below (Eq. (28.2)). Modifying gravity can change the predicted rate of structure growth, and it can make the growth rate dependent on scale or environment. In some circumstances, modifying gravity alters the combinations of potentials responsible for gravitational lensing and the dynamics of non-relativistic tracers (such as galaxies or stars) in different ways (see Sec. 22.4.7 in this *Review*), leading to order unity mismatches between the masses of objects inferred from lensing and those inferred from dynamics in unscreened environments.

At present there are no fully realized and empirically viable modified gravity theories that explain the observed level of cosmic acceleration. The constraints on $f(\mathcal{R})$ models now force them so close to GR that they cannot produce acceleration without introducing a separate dark energy component [18]. The DGP model is empirically ruled out by several tests, including the expansion history, the integrated Sachs-Wolfe effect, and redshift-space distortion measurements of the structure growth rate [19]. The near-simultaneous arrival of gravitational waves and electromagnetic signals from the neutron star merger event GW170817, which shows that gravitational waves travel at almost exactly the speed of light, is a further strong constraint on modified gravity theories [20]. The elimination of models should be considered an important success of the program to empirically test theories of cosmic acceleration. However, it is worth recalling that there was no fully realized gravitational explanation for the precession of Mercury's orbit prior to the completion of GR in 1915, and the fact that no complete and viable modified gravity theory exists today does not mean that one will not arise in the future. In the meantime, we can continue empirical investigations that can tighten restrictions on such theories or perhaps point towards the gravitational sector as the origin of accelerating expansion.

28.2.2 *Expansion History and Growth of Structure*

The main line of empirical attack on dark energy is to measure the history of cosmic expansion and the history of matter clustering with the greatest achievable precision over a wide range of redshift. Within GR, the expansion rate $H(z)$ is governed by the Friedmann equation (see the articles on Big Bang Cosmology and Cosmological Parameters—Secs. 22 and 25.1 in this *Review*). For dark energy with an equation of state $w(z)$, the cosmological constant contribution to the expansion, Ω_Λ, is replaced by a redshift-dependent contribution. The evolution of the dark energy density follows from Eq. (22.10),

$$\Omega_{\rm de}\frac{\rho_{\rm de}(z)}{\rho_{\rm de}(z=0)} = \Omega_{\rm de}\exp\left[3\int_0^z [1+w(z')]\frac{dz'}{1+z'}\right] \; = \; \Omega_{\rm de}(1+z)^{3(1+w)}, \tag{28.1}$$

where the second equality holds for constant w. If $\Omega_{\rm m}$, $\Omega_{\rm r}$, and the present value of $\Omega_{\rm tot}$ are known, then measuring $H(z)$ pins down $w(z)$. (Note that $\Omega_{\rm de}$ is the same quantity denoted $\Omega_{\rm v}$ in Sec. 22, but we have adopted the 'de' subscript to avoid implying that dark energy is necessarily a vacuum effect.)

While some observations can probe $H(z)$ directly, others measure the distance-redshift relation. The basic relations between angular diameter distance or luminosity distance and $H(z)$ are given in Ch. 22 —and these are generally unaltered in time-dependent dark energy or modified gravity models. For convenience, in later sections, we will sometimes refer to the comoving angular distance, $D_{\rm A,c}(z) = (1+z)D_{\rm A}(z)$.

In GR-based linear perturbation theory, the density contrast $\delta(\mathbf{x},t) \equiv \rho(\mathbf{x},t)/\bar{\rho}(t) - 1$ of pressureless matter grows in proportion to the linear growth function $G(t)$ (not to be confused with the gravitational constant $G_{\rm N}$), which follows the differential equation

$$\ddot{G} + 2H(z)\dot{G} - \frac{3}{2}\Omega_{\rm m}H_0^2(1+z)^3 G = 0 \; . \tag{28.2}$$

To a good approximation, the logarithmic derivative of $G(z)$ is

$$f(z) \equiv -\frac{d\ln G}{d\ln(1+z)} \simeq \left[\Omega_{\rm m}(1+z)^3\frac{H_0^2}{H^2(z)}\right]^\gamma \; , \tag{28.3}$$

where $\gamma \simeq 0.55$ for relevant values of cosmological parameters [21]. In an $\Omega_{\rm m} = 1$ Universe, $G(z) \propto (1+z)^{-1}$, but growth slows when $\Omega_{\rm m}$ drops significantly below unity. One can integrate Eq. (28.3) to get an approximate integral relation between $G(z)$ and $H(z)$, but the full (numerical) solution to Eq. (28.2) should be used for precision calculations. Even in the non-linear regime, the amplitude of clustering is determined mainly by $G(z)$, so observations of non-linear structure can be used to infer the linear $G(z)$, provided one has good theoretical modeling to relate the two.

In modified gravity models the growth rate of gravitational clustering may differ from the GR prediction. A general strategy to test modified gravity, therefore, is to measure both the expansion history and the growth history to see whether they yield consistent results for $H(z)$ or $w(z)$.

28.2.3 *Parameters*

Constraining a general history of $w(z)$ is nearly impossible, because the dark energy density, which affects $H(z)$, is given by an integral over $w(z)$, and distances and the growth factor involve a further integration over functions of $H(z)$. Oscillations in $w(z)$ over a range $\Delta z/(1+z) \ll 1$ are therefore extremely difficult to constrain. It has become conventional to phrase constraints or projected constraints on $w(z)$ in terms of a linear evolution model,

$$w(a) = w_0 + w_{\rm a}(1-a) = w_{\rm p} + w_{\rm a}(a_{\rm p} - a), \tag{28.4}$$

where $a \equiv (1+z)^{-1}$, w_0 is the value of w at $z = 0$, and $w_{\rm p}$ is the value of w at a "pivot" redshift $z_{\rm p} \equiv a_{\rm p}^{-1} - 1$, where it is best constrained by a given set of experiments. For typical data combinations, $z_{\rm p} \simeq 0.5$. This simple parameterization can provide a good approximation to the predictions of many physically motivated models for observables measured with percent-level precision. A widely used "Figure of Merit" (FoM) for dark energy experiments [22] is the projected combination of errors $[\sigma(w_{\rm p})\sigma(w_{\rm a})]^{-1}$. Ambitious future experiments with 0.1–0.3% precision on observables can constrain richer descriptions of $w(z)$, which can be characterized by principal components.

There has been less convergence on a standard parameterization for describing modified gravity theories. Deviations from the GR-predicted growth rate can be described by a deviation $\Delta\gamma$ in the index of Eq. (28.3), together with an overall multiplicative offset relative to the $G(z)$ expected from extrapolating the CMB-measured fluctuation amplitude to low redshift. However, these two parameters may not accurately capture the growth predictions of all physically interesting models. Another important parameter to constrain is the ratio of the gravitational potentials governing space curvature and the acceleration of non-relativistic test particles. The possible phenomenology of modified gravity models is rich, which enables many consistency tests but complicates the task of constructing parameterized descriptions.

The more general set of cosmological parameters is discussed elsewhere in this *Review* (Sec. 25.1), but here we highlight a few that are particularly important to the dark energy discussion.

- The dimensionless Hubble parameter $h \equiv H_0/100\ {\rm km\,s^{-1}\,Mpc^{-1}}$ determines the present day value of the critical density and the overall scaling of distances inferred from redshifts.
- $\Omega_{\rm m}$ and $\Omega_{\rm tot}$ affect the expansion history and the distance-redshift relation.
- The sound horizon $r_{\rm s} = \int_0^{t_{\rm rec}} c_{\rm s}(t)dt/a(t)$, the comoving distance that pressure waves can propagate between $t = 0$ and recombination, determines the physical scale of the acoustic peaks in the CMB and the baryon acoustic oscillation (BAO) feature in low-redshift matter clustering [23].
- The amplitude of matter fluctuations, conventionally represented by the quantity $\sigma_8(z)$, scales the overall amplitude of growth measures such as weak lensing or redshift-space distortions (discussed in the next section).

Specifically, $\sigma_8(z)$ refers to the rms fluctuation of the matter overdensity $\rho/\bar{\rho}$ in spheres of radius $8\,h^{-1}$Mpc, computed from the linear theory matter power spectrum at redshift z, and σ_8 on its own refers to the value at $z = 0$ (just like our convention for $\Omega_{\rm m}$).

While discussions of dark energy are frequently phrased in terms of values and errors on quantities like $w_{\rm p}$, $w_{\rm a}$, $\Delta\gamma$, and $\Omega_{\rm tot}$, parameter precision is the means to an end, not an end in itself. The underlying goal of empirical studies of cosmic acceleration is to address two physically profound questions:

- 1. Does acceleration arise from a breakdown of GR on cosmological scales or from a new energy component that exerts repulsive gravity within GR?
- 2. If acceleration is caused by a new energy component, is its energy density constant in space and time, as expected for a fundamental vacuum energy, or does it show variations that indicate a dynamical field?

Substantial progress towards answering these questions, in particular any definitive rejection of the cosmological constant "null hypothesis," would be a major breakthrough in cosmology and fundamental physics.

28.3 Observational Probes

We briefly summarize the observational probes that play the greatest role in current constraints on dark energy. Further discussion can be found in other articles of this *Review*, in particular Secs. 25.1 (Cosmological Parameters) and 29 (The Cosmic Microwave Background), and in Ref. [12], which provides extensive references to background literature. Recent observational results from these methods are discussed in Sec. 28.4.

28.3.1 *Methods, Sensitivity, Systematics*

Cosmic Microwave Background Anisotropies: Although CMB anisotropies provide limited information about dark energy on their own, CMB constraints on the geometry, matter content, and radiation content of the Universe play a critical role in dark energy studies when combined with low-redshift probes. In particular, CMB data supply measurements of $\theta_{\rm s} = r_{\rm s}/D_{\rm A,c}(z_{\rm rec})$, the angular size of the sound horizon at recombination, from the angular location of the acoustic peaks, measurements of $\Omega_{\rm m}h^2$ and $\Omega_{\rm b}h^2$ from the heights of the peaks, and normalization of the amplitude of matter fluctuations at $z_{\rm rec}$ from the amplitude of the CMB fluctuations themselves. *Planck* data yield a 0.18% determination of $r_{\rm s}$, which scales as $(\Omega_{\rm m}h^2)^{-0.25}$ for cosmologies with standard matter and radiation content. The uncertainty in the matter fluctuation amplitude at the epoch of recombination is 0.5%. Secondary anisotropies, including the integrated Sachs-Wolfe effect, the Sunyaev-Zeldovich (SZ, [24]) effect, and weak lensing of primary anisostropies, provide additional information about dark energy by constraining low-redshift structure growth.

Type Ia Supernovae (SN): Type Ia supernovae, produced by the thermonuclear explosions of white dwarfs, exhibit 10–15% scatter in peak luminosity after correction for light curve duration (the time to rise and fall) and color (which is a diagnostic of dust extinction). Since the peak luminosity is not known *a priori*, supernova surveys constrain ratios of luminosity distances at different redshifts. If one is comparing a high-redshift sample to a local calibrator sample measured with much higher precision (and distances inferred from Hubble's law), then one essentially measures the luminosity distance in h^{-1}Mpc, constraining the combination $hD_{\rm L}(z)$. With distance uncertainties of 5–8% per well observed supernova, a sample of around 100 SNe is sufficient to achieve sub-percent statistical precision. The 1–2% systematic uncertainties in current samples are dominated by uncertainties associated with photometric calibration and dust extinction corrections plus the observed dependence of luminosity on host galaxy properties. Another potential systematic is redshift evolution of the supernova population itself, which can be tested by analyzing subsamples grouped by spectral properties or host galaxy properties to confirm that they yield consistent results.

Baryon Acoustic Oscillations (BAO): Pressure waves that propagate in the pre-recombination photon-baryon fluid imprint a characteristic scale in the clustering of matter and galaxies, which appears in the galaxy correlation function as a localized peak at the sound horizon scale $r_{\rm s}$, or in the power spectrum as a series of oscillations. Since observed galaxy coordinates consist of angles and redshifts, measuring this "standard ruler" scale in a galaxy redshift survey determines the angular diameter distance $D_A(z)$ and the expansion rate $H(z)$, which convert coordinate separations to comoving distances. Errors on the two quantities are correlated, and in existing galaxy surveys the best determined combination is approximately $D_V(z) = [czD_{A,c}^2(z)/H(z)]^{1/3}$. As an approximate rule of thumb, a survey that fully samples structures at redshift z over a comoving volume V, and is therefore limited by cosmic variance rather than shot noise, measures $D_{A,c}(z)$ with a fractional error of $0.005(V/10\,\mathrm{Gpc}^3)^{-1/2}$ and $H(z)$ with a fractional error 1.6–1.8 times higher. The most precise BAO measurements to date come from large galaxy redshift surveys probing $z < 0.8$, and these will be extended to higher redshifts by future projects. At redshifts $z > 2$, BAO can also be measured in the Lyman-α forest of intergalactic hydrogen absorption towards background quasars, where the fluctuating absorption pattern provides tens or hundreds of samples of the density field along each quasar sightline. For Lyman-α forest BAO, the best measured parameter combination is more heavily weighted towards $H(z)$ because of strong redshift-space distortions that enhance clustering in the line-of-sight direction. Radio intensity mapping, which maps large-scale structure in redshifted 21-cm hydrogen emission without resolving individual galaxies, offers a potentially promising route to measuring BAO over large volumes at relatively low cost, but the technique is still under development. Photometric redshifts in optical imaging surveys can be used to measure BAO in the angular direction, though the typical distance precision is a factor of 3–4 lower compared to a well sampled spectroscopic survey of the same area, and angular BAO measurements do not directly constrain $H(z)$. BAO distance measurements complement SN distance measurements by providing absolute rather than relative distances (with precise calibration of r_s from the CMB) and by having greater achievable precision at high redshift thanks to the increasing comoving volume available. Theoretical modeling suggests that BAO measurements from even the largest feasible redshift surveys will be limited by statistical rather than systematic uncertainties.

Weak Gravitational Lensing: Gravitational light bending by a clustered distribution of matter shears the shapes of higher redshift background galaxies in a spatially coherent manner, producing a correlated pattern of apparent ellipticities. By studying the weak lensing signal for source galaxies binned by photometric redshift (estimated from broad-band colors), one can probe the history of structure growth. "Cosmic shear" weak lensing uses the correlation of source ellipticities to deduce the clustering of intervening matter. "Galaxy-galaxy lensing" (GGL) uses the correlation between a shear map and a foreground galaxy sample to measure the average mass profile around the foreground galaxies, which can be combined with galaxy clustering to constrain total matter clustering. For a specified expansion history, the predicted signals scale approximately as $\sigma_8\Omega_m^\alpha$, with $\alpha \simeq 0.3$–0.5. The predicted signals also depend on the distance-redshift relation, so weak lensing becomes more powerful in concert with SN or BAO measurements that can pin this relation down independently. The most challenging systematics are shape measurement biases, biases in the distribution of photometric redshifts, and intrinsic alignments of galaxy orientations that could contaminate the lensing-induced signal. Weak lensing of CMB anisotropies is an increasingly powerful tool, in part because it circumvents many of these observational and astrophysical systematics. Predicting the large-scale weak lensing signal is straightforward in principle, but the number of independent modes on large scales is small, and the inferences are therefore dominated by sample variance. Exploiting small-scale measurements, for tighter constraints, requires modeling the effects of complex physical processes such as star formation and feedback on the matter power spectrum. Strong gravitational lensing can also provide constraints on dark energy, either through time delay measurements that probe the absolute distance scale, or through measurements of multiple-redshift lenses that constrain distance ratios. The primary uncertainty for strong lensing constraints is modeling the mass distribution of the lens systems.

Clusters of Galaxies: Like weak lensing, the abundance of massive dark-matter halos probes struc-

Table 28.1: A selection of major dark-energy experiments, based on Ref. [25]. Abbreviations in the "Data" column refer to optical (Opt) or near-infrared (NIR) imaging (I) or spectroscopy (S). For spectroscopic experiments, the "Spec-z" column lists the primary redshift range for galaxies (gals), quasars (QSOs), or the Lyman-α forest (LyαF). Abbreviations in the "Methods" column are weak lensing (WL), clusters (CL), supernovae (SN), baryon acoustic oscillations (BAO), and redshift-space distortions (RSD).

Project	Dates	Area/deg^2	Data	Spec-z Range	Methods
BOSS	2008–2014	10,000	Opt-S	0.3–0.7 (gals)	BAO/RSD
				2–3.5 (LyαF)	
KiDS	2011–2019	1500	Opt-I	——	WL/CL
DES	2013–2019	5000	Opt-I	——	WL/CL
					SN/BAO
eBOSS	2014–2018	7500	Opt-S	0.6–2.0 (gal/QSO)	BAO/RSD
				2–3.5 (LyαF)	
SuMIRE	2014–2024	1500	Opt-I		WL/CL
			Opt/NIR-S	0.8–2.4 (gals)	BAO/RSD
HETDEX	2017–2023	450	Opt-S	$1.9 < z < 3.5$ (gals)	BAO/RSD
DESI	2020–2025	14,000	Opt-S	0–1.7 (gals)	BAO/RSD
				2–3.5 (LyαF)	
LSST	2022–2032	20,000	Opt-I	——	WL/CL
					SN/BAO
Euclid	2022–2028	15,000	Opt-I		WL/CL
			NIR-S	0.7–2.2 (gals)	BAO/RSD
WFIRST	2025–2030	2200	NIR-I		WL/CL/SN
			NIR-S	1.0–3.0 (gals)	BAO/RSD

ture growth by constraining $\sigma_8\Omega_{\rm m}^{\alpha}$, where $\alpha \simeq 0.3$–0.5. These halos can be identified as dense concentrations of galaxies or through the signatures of hot (10^7–10^8 K) gas in X-ray emission or SZ distortion of the CMB. The critical challenge in cluster cosmology is calibrating the relation $P(M_{\rm halo}|O)$ between the halo mass as predicted from theory and the observable O used for cluster identification. Measuring the stacked weak lensing signal from clusters has emerged as a promising approach to achieve percent-level accuracy in calibration of the mean relation, which is required for clusters to remain competitive with other growth probes. This method requires accurate modeling of completeness and contamination of cluster catalogs, projection effects on cluster selection and weak lensing measurements, and possible baryonic physics effects on the mass distribution within clusters.

Redshift-Space Distortions (RSD) and the Alcock-Paczynksi (AP) Effect: Redshift-space distortions of galaxy clustering, induced by peculiar motions, probe structure growth by constraining the parameter combination $f(z)\sigma_8(z)$, where $f(z)$ is the growth rate defined by Eq. (28.3). Uncertainties in theoretical modeling of non-linear gravitational evolution and the non-linear bias between the galaxy and matter distributions currently limit application of the method to large scales (comoving separations $r \gtrsim 10\,h^{-1}$Mpc or wavenumbers $k \lesssim 0.2h\,{\rm Mpc}^{-1}$). A second source of anisotropy arises if one adopts the wrong cosmological metric to convert angles and redshifts into comoving separations, a phenomenon known as the Alcock-Paczynksi effect [26]. Demanding isotropy of clustering at redshift z constrains the parameter combination $H(z)D_A(z)$. The main challenge for the AP method is correcting for the anisotropy induced by peculiar velocity RSD.

Low Redshift Measurement of H_0: The value of H_0 sets the current value of the critical density $\rho_c = 3H_0^2/8\pi G_N$, and combination with CMB measurements provides a long lever arm for constraining the evolution of dark energy. The challenge in conventional H_0 measurements is establishing distances to galaxies that are "in the Hubble flow," *i.e.*, far enough away that their peculiar velocities are small compared to the expansion velocity $v = H_0 d$. This can be done by building a ladder of distance indicators tied to stellar parallax on its lowest rung, or by using gravitational-lens time delays or geometrical measurements of maser data to circumvent this ladder.

28.3.2 *Dark Energy Experiments*

Most observational applications of these methods now take place in the context of large cosmological surveys, for which constraining dark energy and modified gravity theories is a central objective. Table 28.1 lists a selection of current and planned dark-energy experiments, taken originally from the Snowmass 2013 Dark Energy Facilities review [25], which focused on projects in which the U.S. has either a leading role or significant participation. References and links to further information about these projects can be found in Ref. [25]. We have adjusted some of the dates in this Table relative to those in Ref. [25] and added the European-led KiloDegree Survey (KiDS). Dates in the Table correspond to the duration of survey observations, and the final cosmological results frequently require 1–3 years of analysis and modeling beyond the end of data taking.

Beginning our discussion with imaging surveys, the Dark Energy Survey (DES) has observed 1/8 of the sky to a depth roughly 2 magnitudes deeper than the Sloan Digital Sky Survey (SDSS), enabling weak lensing measurements with much greater statistical precision, cluster measurements calibrated by weak lensing, and angular BAO measurements based on photometric redshifts. With repeat imaging over a smaller area, DES has identified thousands of Type Ia SNe, which together with spectroscopic follow-up data enable significant improvements on the current state-of-the-art for supernova (SN) cosmology. Cosmological results from weak lensing and galaxy clustering analyses of the first year DES data are presented in Ref. [27] and discussed further below, while the first cosmological results from the DES supernova survey are presented in Ref. [28]. The Hyper-Suprime Camera (HSC) on the Subaru 8.2-m telescope is carrying out a similar type of optical imaging survey, probing a smaller area than DES but to greater depth. First cosmological results from HSC weak lensing are reported in Refs. [29, 30]. The HSC survey is one component of the Subaru Measurement of Images and Redshifts (SuMIRE) project. Beginning in the early 2020s, the dedicated Large Synoptic Survey Telescope (LSST) will scan the southern sky to SDSS-like depth every four nights. LSST imaging co-added over its decade-long primary survey will reach extraordinary depth, enabling weak lensing, cluster, and photometric BAO studies from billions of galaxies. Additionally, LSST time-domain monitoring will identify and measure light curves for thousands of Type Ia SNe per year.

Turning to spectroscopic surveys, the Baryon Oscillation Spectroscopic Survey (BOSS) and its successor eBOSS used fiber-fed optical spectrographs to map the redshift-space distributions of millions of galaxies and quasars. These 3-dimensional maps enable BAO and RSD measurements, and Lyman-α forest spectra of high-redshift quasars extend these measurements to redshifts $z > 2$. As discussed below, the BOSS Collaboration has now published BAO and RSD analyses of its final data sets, and eBOSS has released BAO measurements from quasar clustering at $z = 1$–2. The Hobby-Eberly Telescope Dark Energy Experiment (HETDEX) uses integral field spectrographs to detect Lyman-α emission-line galaxies at $z \simeq 1.9$–3.5, probing a small sky area but a substantial comoving volume. The Dark Energy Spectroscopic Instument (DESI) will follow a strategy similar to BOSS/eBOSS but on a much grander scale, using a larger telescope (4-m vs. 2.5-m) and a much higher fiber multiplex (5000 vs. 1000) to survey an order-of-magnitude more galaxies. A new Prime Focus Spectrograph (PFS) for the Subaru telescope will enable the spectroscopic component of SuMIRE, with the large telescope aperture and wavelength sensitivity that extends to the near-infrared (NIR) allowing it to probe a higher redshift galaxy population than DESI, over a smaller area of sky.

Compared to ground-based observations, space observations afford higher angular resolution and a far lower NIR sky background. The *Euclid* and *WFIRST* (*Wide Field Infrared Survey Telescope*) missions will exploit these advantages, conducting large area imaging surveys for weak lensing and cluster studies and slitless spectroscopic surveys of emission-line galaxies for BAO and RSD studies. *WFIRST* will also incorporate an imaging and spectrophotometric supernova (SN) survey, extending to redshift $z \simeq 1.7$. Survey details are likely to evolve prior to launch, but in the current designs one can roughly characterize the difference between the *Euclid* and *WFIRST* dark-energy experiments as "wide vs. deep," with planned survey areas of 15,000 deg^2 and 2200 deg^2, respectively. For weak lensing shape measurements, *Euclid* will use a single wide optical filter, while *WFIRST* will use three NIR filters. The *Euclid* galaxy redshift survey will cover a large volume at relatively low space density, while the *WFIRST* survey will provide denser sampling of structure in a smaller volume. There are numerous synergies among the LSST, *Euclid*, and *WFIRST* dark energy programs, as discussed in Ref. [31].

28.4 Current Constraints on Expansion, Growth, and Dark Energy

The last decade has seen dramatic progress in measurements of the cosmic expansion history and structure growth, leading to much tighter constraints on the parameters of dark energy models. CMB data from the *WMAP* and *Planck* satellites and from higher resolution ground-based experiments have provided an exquisitely detailed picture of structure at the recombination epoch and the first CMB-based measures of low-redshift structure through lensing and SZ cluster counts. Cosmological supernova samples have increased in size from tens to many hundreds, with continuous coverage from $z = 0$ to $z \simeq 1.4$, alongside major improvements in data quality, analysis methods, and detailed understanding of local populations. BAO measurements have advanced from the first detections to 1–2% precision at multiple redshifts, with increasingly sophisticated methods for testing systematics, fitting models, and evaluating statistical errors. Advances in X-ray, SZ, and weak-lensing observations of large samples of galaxy clusters allow a multi-faceted approach to mass calibration, improving statistical precision but also revealing sources of astrophysical uncertainty. Cluster constraints have been joined by the first precise matter-clustering constraints from cosmic-shear weak lensing and galaxy-galaxy lensing, and by redshift-space distortion measurements that probe different aspects of structure growth at somewhat lower precision. The precision of low-redshift H_0 measurements has sharpened from the roughly 10% error of the *HST* Key Project [32] to 2–4% in recent analyses.

As an illustration of current measurements of the cosmic expansion history, Fig. 28.1 compares distance-redshift measurements from SN and BAO data to the predictions for a flat Universe with a cosmological constant. SN cosmology relies on compilation analyses that try to bring data from different surveys probing distinct redshift ranges to a common scale. Here we use the "joint light curve analysis" (JLA) sample of Ref. [34], who carried out a careful intercalibration of the 3-year Supernova Legacy Survey (SNLS3, [35]) and the full SDSS-II Supernova Survey [3] data in combination with several local supernova samples and high-redshift supernovae from *HST*. Results from the Union2.1 sample [36], which partly overlaps JLA but has different analysis procedures, would be similar. Other state-of-the-art supernova data sets include the Pan-STARRS1 sample incorporated in the PANTHEON compilation [37] and the first sample of spectroscopically confirmed supernovae from DES [28]. For illustration purposes, we have binned the JLA data in redshift and plotted the

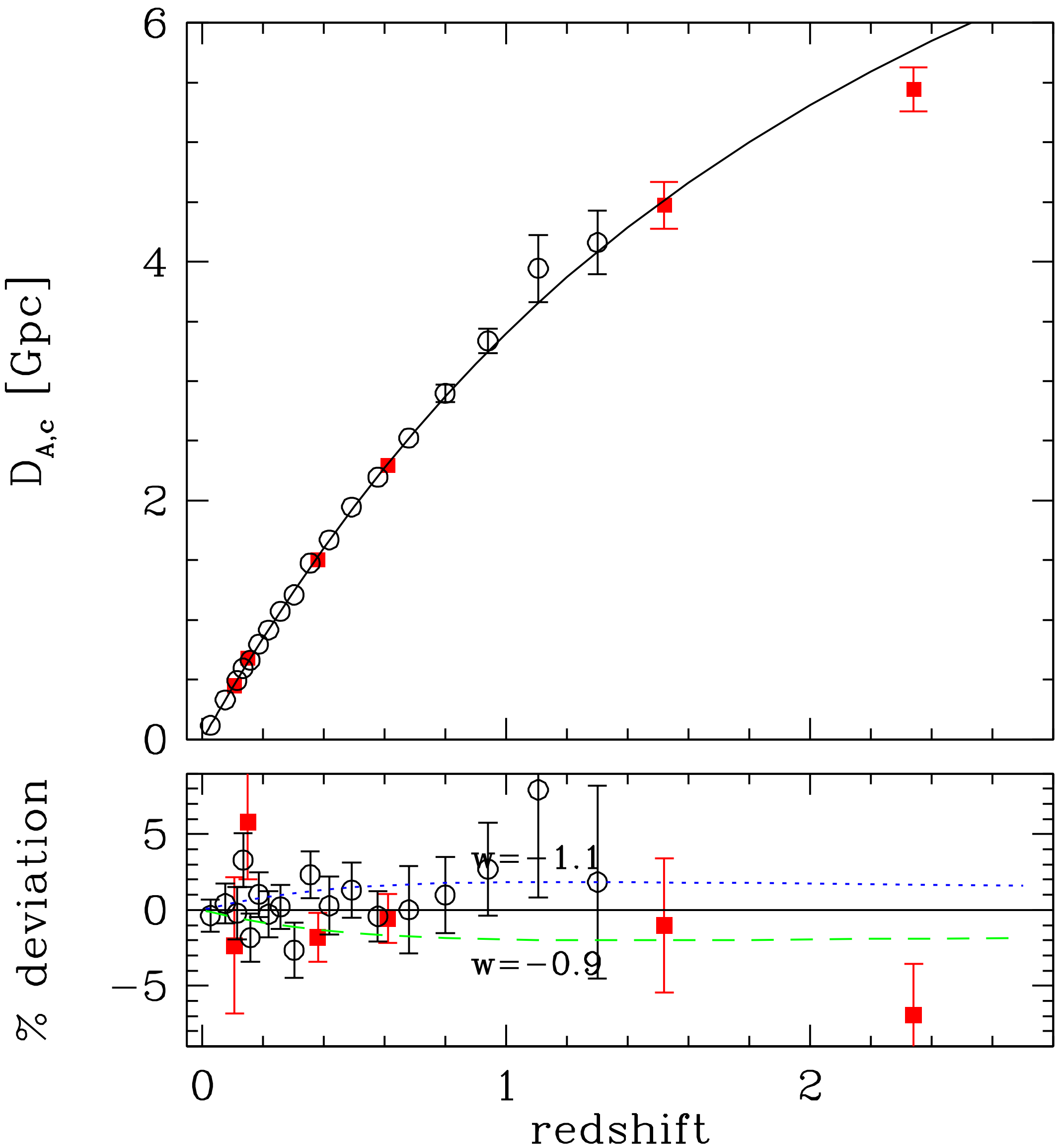

Figure 28.1: Distance-redshift relation measured from Type Ia SNe and BAO compared to the predictions (black curve) of a flat ΛCDM model with $\Omega_m = 0.315$ and $h = 0.674$, the best-fit parameters inferred from *Planck* CMB data [33]. Circles show binned luminosity distances from the JLA SN sample [34], multiplied by $(1+z)^{-1}$ to convert to comoving angular diameter distance. Red squares show BAO distance measurements from the 6dFGS, SDSS-II, BOSS, and eBOSS surveys (see text for details and references). The lower panel plots residuals from the ΛCDM prediction, with dashed and dotted curves that show the effect of changing w by ± 0.1 while all other parameters are held fixed. Note that the SN data points can be shifted up or down by a constant factor to account for freedom in the peak luminosity, while the BAO points are calibrated to 0.2% precision by the sound horizon scale computed from *Planck* data. The errors on the BAO data points are approximately independent. In the upper panel, error bars are plotted only at $z > 0.7$ to avoid visual confusion.

diagonal elements of the covariance matrix as error bars, and we have converted the SN luminosity distances to an equivalent comoving angular diameter distance. Because the peak luminosity of a fiducial SN Ia is an unknown free parameter, the SN distance measurements could all be shifted up and down by a constant multiplicative factor; cosmological information resides in the relative distances as a function of redshift. The normalization used here corresponds to a Hubble parameter $h = 0.674$.

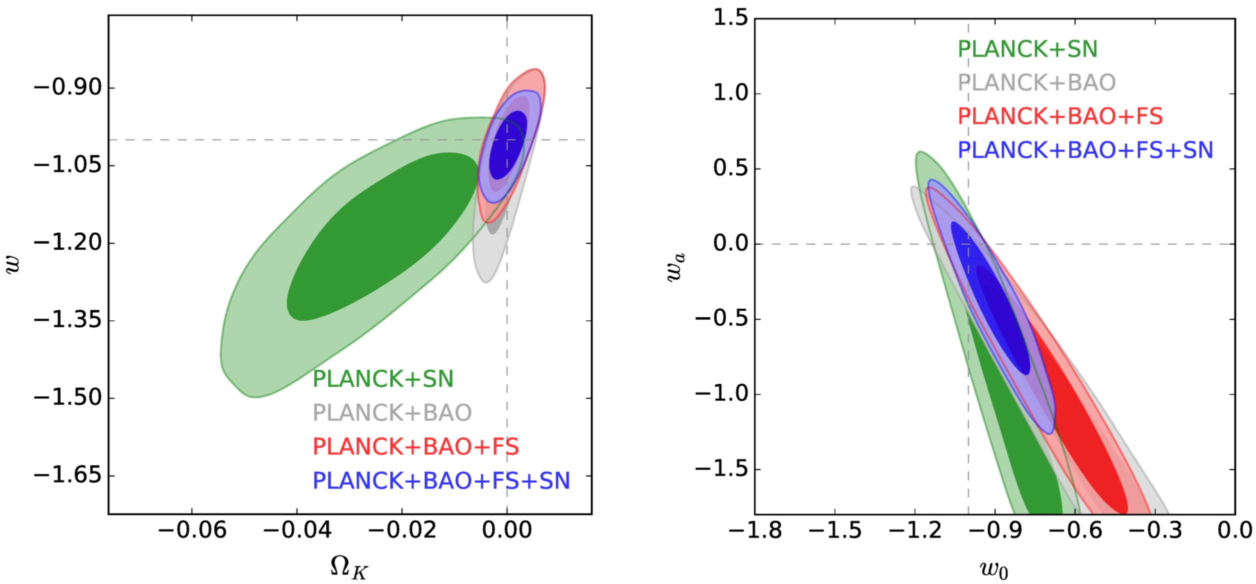

Figure 28.2: Constraints on dark energy model parameters from combinations of CMB, BAO, galaxy clustering, and supernova (SN) data, taken from Ref. [38]. The left panel shows 68% and 95% confidence contours in the `owCDM` model, with constant equation-of-state parameter w and non-zero space curvature $\Omega_K \equiv 1 - \Omega_{\rm tot}$. Green and gray contours show the combination of *Planck* CMB data with SN or BAO data, respectively. Red contours combine CMB, BAO, and the full shape (FS) of redshift-space galaxy clustering. Blue contours add SN data to this combination. The right panel shows confidence contours for the same data combinations in the $\mathtt{w_0w_a}$CDM model, which assumes a flat Universe and an evolving equation of state with $w(a) = w_0 + w_{\rm a}(1 - a)$.

The $z < 2$ BAO data points come from the 6-degree-Field Galaxy Survey 6dFGS survey [39], the SDSS-II Main Galaxy Sample [40], the final galaxy clustering data set from BOSS [38], and the first BAO measurement from quasar clustering in eBOSS [41]. For the 6dFGS, SDSS-II, and eBOSS data points, values of $D_{\rm V}$ have been converted to $D_{\rm A,c}$. The BOSS analysis measures $D_{\rm A,c}$ directly; we have taken values from the "BAO only" column of table 7 of Ref. [38]. At $z = 2.34$ we plot $D_{\rm A,c}$ measured from the BAO analysis of the eBOSS Lyman-α forest auto-correlation and cross-correlation with quasars [42]. The BAO measurements are converted to absolute distances using the sound horizon scale $r_{\rm s} = 147.09$ Mpc from *Planck* 2018 CMB data, whose 0.18% uncertainty is small compared to the current BAO measurement errors. The BOSS galaxy and eBOSS Lyman-α forest analyses also measure $H(z)$ at the same redshifts, providing further leverage on expansion history that is not captured in Fig. 28.1.

The plotted cosmological model has $\Omega_{\rm m} = 0.315$ and $h = 0.674$, the best-fit values from *Planck* (TT+TE+EE+lowE+lensing) assuming $w = -1$ and $\Omega_{\rm tot} = 1$ [33]. The SN, BAO, and CMB data sets, probing a wide range of redshifts with radically different techniques, are for the most part mutually consistent with the predictions of a flat ΛCDM cosmology. The eBOSS Lyman-α forest BAO measurements lie about 1.7σ from the *Planck* ΛCDM prediction [42], notably closer than the 2.3σ difference obtained with earlier BOSS data and discussed in the 2018 edition of this

Review. Dotted and dashed curves in the lower panel of Fig. 28.1 show the effect of changing w by ± 0.1 with all other parameters held fixed, which leads to significantly worse agreement with the data. However, such a single-parameter comparison does not capture the impact of parameter degeneracies or the ability of complementary data sets to break them, and if one instead forced a match to CMB data by changing h and $\Omega_{\rm m}$ when changing w then the predicted BAO distances would diverge at $z = 0$ rather than converging there.

Figure 28.2, taken from Ref. [38], presents constraints on models that allow a free but constant value of w with non-zero space curvature (`owCDM`, left panel) or the evolving equation of state of Eq. (28.4) in a flat Universe ($\texttt{w}_0\texttt{w}_a\texttt{CDM}$, right panel). Green contours show constraints from the combination of *Planck* 2015 CMB data and the JLA supernova sample. Gray contours show the combination of *Planck* with BAO measurements from BOSS, 6dFGS, and SDSS-II. Red contours adopt a more aggressive analysis of the BOSS galaxy data that uses the full shape (FS) of the redshift-space power spectrum and correlation function, modeled via perturbation theory, in addition to the measurement of the BAO scale itself. The full shape analysis improves the constraining power of the data, primarily because measurement of the Alcock-Paczynski effect on sub-BAO scales helps to break the degeneracy between $D_{\rm A,c}(z)$ and $H(z)$. Blue contours show constraints from the full combination of CMB, BAO+FS, and SN data. Supernovae provide fine-grained relative distance measurements with good bin-by-bin precision at $z < 0.7$ (see Fig. 28.1), which is complementary to BAO for constraining redshift evolution of w. In both classes of model, the flat ΛCDM parameters ($w = w_0 = -1$, $\Omega_{\rm K} = w_{\rm a} = 0$) lie within the 68% confidence contour.

The precision on dark energy parameters depends, of course, on both the data being considered and the flexibility of the model being assumed. For the `owCDM` model and the Planck+BAO+FS+SN data combination, Ref. [38] finds $w = -1.01 \pm 0.04$. Assuming a flat Universe and incorporating *Planck* 2018 data and DES Year 1 weak lensing, in addition to BAO and SN, Ref. [33] finds

$$w = -1.028 \pm 0.031 \ . \tag{28.5}$$

We consider either of these results to be a reasonable characterization of current knowledge about the dark energy equation of state. In the $\texttt{w}_0\texttt{w}_a\texttt{CDM}$ model there is strong degeneracy between w_0 and $w_{\rm a}$, as one can see in Fig. 28.2. However, the value of w at the pivot redshift $z_{\rm p} = 0.29$ is well constrained by the Planck+BAO+FS+SN data combination, with $w_{\rm p} = -1.05 \pm 0.06$ [38]. The constraint on the evolution parameter, by contrast, remains poor even with this data combination, $w_{\rm a} = -0.39 \pm 0.34$. For examinations of a wide range of dark energy, dark matter, neutrino content, and modified gravity models, see Refs. [33, 38, 43].

A flat ΛCDM model fit to *Planck* CMB data alone predicts $H_0 = 67.4 \pm 0.5\ {\rm km\,s^{-1}\,Mpc^{-1}}$ (see Chapter 29 of this *Review*). This prediction and its error bar are sensitive to the assumptions of constant dark energy and a flat Universe. However, by adding BAO and supernova data one can construct an "inverse distance ladder" to measure H_0 precisely, even with a general dark energy model and free curvature [44]. Ref. [45] applies this approach to obtain $H_0 = 67.8 \pm 1.3\ {\rm km\,s^{-1}\,Mpc^{-1}}$. As discussed in Sec. 25.3.1of this *Review*, recent measurements from low-redshift data yield higher values of H_0. Figure 28.3 compares the CMB-anchored H_0 estimates cited above to distance-ladder estimates that use Cepheid [46] or tip-of-the-red-giant-branch (TRGB) [47] stars to calibrate SNe Ia luminosities, and to an entirely independent estimate that uses gravitational-lens time delays [48]. The Cepheid and lensing estimates are discrepant with the CMB-anchored estimates at a statistically significant level (Ref. [46] quotes 4.4σ relative to *Planck* ΛCDM), while the TRGB calibration yields an intermediate result that is consistent with either the "high" or "low" values of H_0.

The tension in H_0 could reflect some combination of statistical flukes and systematic errors in one or more of the data sets employed in these analyses. However, if the resolution lies in new physics rather than measurement errors, then this is probably physics that operates in the *pre-recombination* Universe, rescaling the BAO standard ruler in a way that shifts the ΛCDM and inverse-distance-ladder values upward. Models with extra relativistic degrees of freedom or dark energy that is dynamically significant in the early Universe can achieve this effect by increasing the early expansion rate, but they are tightly constrained by the damping tail of CMB anisotropies. A finely tuned model in which early dark energy decays rapidly after recombination can mitigate the tension between CMB data and local H_0 measurements [49], though it still prefers H_0 values below those of Ref. [46].

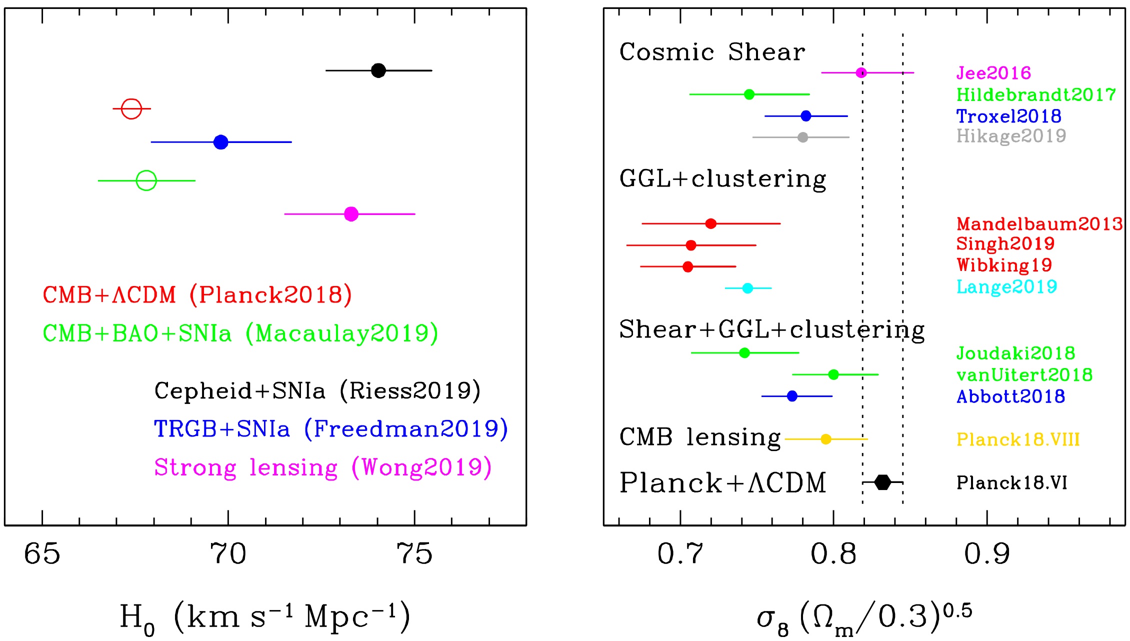

Figure 28.3: Tensions between low-redshift cosmological measurements and the predictions of a CMB-normalized ΛCDM model. All error bars are 1σ; see text for observational references. *(Left)* Open circles show values of H_0 for flat ΛCDM with *Planck* parameters or a general dark energy model constrained by a combination of CMB, BAO, and supernova data. Filled circles show distance-ladder estimates based on Cepheid or TRGB calibration or an independent estimate using gravitational-lens time delays. *(Right)* Matter clustering characterized by the parameter combination $\sigma_8(\Omega_m/0.3)^{0.5}$, as predicted by a *Planck*-normalized ΛCDM model (vertical dotted lines, black hexagon) and estimated from weak gravitational lensing using cosmic shear, galaxy-galaxy lensing and galaxy clustering, or a combination of the two constraints. Points of the same color are based on the same weak-lensing data. The "CMB lensing" point shows the value of σ_8 for $\Omega_m = 0.3$ inferred from *Planck* CMB lensing, a measurement that is independent of the "Planck+ΛCDM" prediction and weighted to somewhat higher redshift than the other weak-lensing points.

The amplitude of CMB anisotropies is proportional to the amplitude of density fluctuations present at recombination, and by assuming GR and a specified dark energy model one can extrapolate the growth of structure forward to the present day to predict σ_8. Probes of low-redshift structure yield constraints in the (σ_8, Ω_m) plane, which can be summarized in terms of the parameter combination $S_8 \equiv \sigma_8(\Omega_m/0.3)^{0.5}$. As discussed in earlier editions of this *Review*, many but not all weak-lensing and cluster studies to date yield S_8 values lower than those predicted for *Planck*-normalized ΛCDM. The right panel of Fig. 28.3 illustrates the current state-of-play, comparing a selection of recently published S_8 estimates to the *Planck*+ΛCDM prediction of $S_8 = 0.832 \pm 0.013$.

The first four points show cosmic-shear weak-lensing estimates from the Deep Lens Survey [50], KiDS [51], DES [52], and HSC [29]. All of these estimates lie below the *Planck* central value, though only the KiDS estimate is discrepant by $\sim 2\sigma$. The next four points use galaxy-galaxy lensing in combination with galaxy clustering. Ref. [53] used weak-lensing data from SDSS imaging and the SDSS main galaxy redshift catalog, restricting the analysis to scales well described by perturbation theory. Refs. [54] and [55] used the same weak-lensing data but the BOSS LOWZ galaxy sample, and they employed two quite different approaches to model the clustering and lensing signals into the strongly non-linear regime ($r \approx 1\,h^{-1}$Mpc) so that they could fully exploit the constraining power of the data. Ref. [56] found a strong discrepancy on these non-linear scales between the predictions of a *Planck*-normalized ΛCDM model and the galaxy-galaxy lensing of BOSS CMASS galaxies, measured from 250 deg^2 of deep imaging from the Canada-France-Hawaii Telescope. Ref. [57], plotted in Figure 28.3, revisited these data with a more general modeling approach and showed that the discrepancy persists over a range of redshift and galaxy stellar mass.

The third set of points in this panel shows S_8 estimates that combine cosmic shear with galaxy-galaxy lensing and galaxy clustering (a.k.a. "3×2" analyses because they combine three 2-point correlations), restricted to fairly large scales in the perturbative regime. Refs. [58] and [59] use KiDS weak-lensing data but two different galaxy samples; although they are statistically consistent with each other, the difference of their central values illustrates the sensitivity to external data and analysis choices. Ref. [27] presents constraints from the 3×2 analysis of the Year 1 DES data, which yields an S_8 value lower than the Planck prediction but consistent at the $\sim 2\sigma$ level.

The "CMB lensing" point shows the matter-clustering amplitude inferred from *Planck* CMB lensing; we have evaluated Eq. (38) of Ref. [60] at $\Omega_{\rm m} = 0.3$ and adopted the same fractional error. It is important to emphasize that this is a measurement of low-redshift clustering even though the background being lensed is the CMB. The CMB lensing kernels peak at $z \lesssim 1$, with tails to $z \sim 5$, so the effective redshift of the S_8 measurement is somewhat higher than that of the other weak-lensing data points. The result is consistent with the *Planck*+ΛCDM prediction at 1σ, and it is also consistent with the lower value corresponding to the mean or median of the optical weak-lensing measurements.

No one of these analyses provides convincing evidence of a conflict with the ΛCDM cosmological model. However, the case for such a conflict has grown stronger as the low inferred clustering amplitude has persisted across multiple statistically independent weak-lensing surveys and multiple analysis methods. One possible explanation is that several of the weak lensing surveys are affected by a common, unrecognized, systematic bias. Another possibility is a true deviation between the clustering growth extrapolated forward from the early Universe and the clustering of matter at late times. The consistency of CMB lensing and Lyman-α forest measurements with ΛCDM clustering predictions suggests that any such deviation sets in mainly at $z < 1$, coinciding with the era of cosmic acceleration. Because the expansion history is well constrained by BAO and supernova data, it is difficult to change low-redshift matter clustering by simply changing the equation of state of dark energy. Instead, a deviation between predicted and observed clustering might point towards modified gravity, decaying dark matter, or coupling between dark matter and dark energy.

The next 2–3 years should see rapid progress on this conundrum. As the KiDS, DES, and HSC data sets grow in size, their statistical uncertainties will shrink, which will in turn enable more stringent internal cross-checks that test for consistent results from different redshift ranges, different scales, and different lens and source populations. Modeling methods that exploit non-linear scales will also be more stringently tested. Clusters of galaxies with weak-lensing mass calibration provide an alternative route to S_8 measurement, with competitive statistical precision. Recent cluster-based S_8 estimates span a wide range, some of them consistent with *Planck*+ΛCDM and others implying lower matter clustering, and we have not quoted results here because it is difficult to decide which are most reliable. However, the opportunity to combine multiple cluster samples with multiple weak-lensing surveys may lead to consistent and convincing measurements in the near future. CMB lensing constraints will improve with higher angular resolution data from the South Pole Telescope and the Atacama Cosmology Telescope and their successors. Finally, the DESI survey will soon allow the first RSD-based measurements of structure growth at the 1–2% level, providing an entirely distinct route to probe the clustering tension hinted at in Fig. 28.3.

28.5 Summary and Outlook

Figure 28.2 focuses on model parameter constraints, but to describe the observational situation it is more useful to characterize the precision, redshift range, and systematic uncertainties of the basic expansion and growth measurements. At present, supernova surveys constrain distance ratios at the 1–2% level in redshift bins of width $\Delta z = 0.1$ over the range $0 < z < 0.6$, with larger but still interesting error bars out to $z \simeq 1.3$. These measurements are currently limited by systematics tied to photometric calibration, dust reddening, host-galaxy correlations, and possible evolution of the SN population. BAO surveys have measured the absolute distance scale (calibrated to the sound horizon r_s) to 4% at $z = 0.15$, 1% at $z = 0.38$ and $z = 0.61$, and 2% at $z = 2.3$. Multiple studies have used clusters of galaxies or weak-lensing cosmic shear or galaxy-galaxy lensing to measure a parameter combination $\sigma_8 \Omega_\mathrm{m}^\alpha$ with $\alpha \simeq 0.3$–0.5. The estimated errors of the most recent studies, including both statistical contributions and identified systematic uncertainties, are 3–5%. RSD measurements constrain the combination $f(z)\sigma_8(z)$, and recent determinations span the redshift range $0 < z < 0.9$ with typical estimated errors of about 10%. These errors are dominated by statistics, but shrinking them further will require improvements in modeling non-linear effects on small scales. Distance-ladder estimates of H_0 now span a small range, using overlapping data but distinct treatments of key steps; individual studies quote uncertainties of 2–5%, with similar statistical and systematic contributions. *Planck* data and higher resolution ground-based experiments now measure CMB anisotropies with exquisite precision; for example, CMB measurements now constrain the physical size of the BAO sound horizon to 0.2% and the angular scale of the sound horizon to 0.01%.

A flat ΛCDM model with standard radiation and neutrino content can fit the CMB data and the BAO and SN distance measurements to within their estimated uncertainties. The CMB+BAO parameters for this model are in significant tension with some but not all recent measurements of H_0 determined from low-redshift data. The discrepancy could reflect underestimated systematic errors in one or more of the input data sets. If the conflict is real, then it may point to new physics in the pre-recombination Universe that rescales the sound horizon, such as early dark energy or extra relativistic degrees of freedom. Many measurements of low-redshift matter clustering from weak lensing lie below the predictions of a ΛCDM model extrapolated forward from the *Planck* CMB anisotropies. No one analysis presents a convincing conflict, but the difference persists across several independent data sets and analysis methods. If real, this discrepancy could point towards modified gravity, decaying dark matter, or coupling between dark matter and dark energy. However, none of the tensions present in the data yet provides compelling evidence for new physics.

Analyses of the final KiDS and DES weak-lensing data sets and the expanding HSC weak-lensing data set should yield measurements of matter clustering that have sharper statistical precision and more stringent tests of internal consistency. Fully exploiting these data will require further development of accurate models of matter clustering, galaxy clustering, and weak lensing by galaxy clusters into the fully non-linear regime, including robust methods of accounting for uncertainties in the baryonic mass distribution. It will also require further progress on the thorny challenge of photometric redshift calibration so that these uncertainties do not dominate the error budget. Higher signal-to-noise CMB lensing maps cross-correlated with galaxies will provide independent tests that avoid some of the systematic uncertainties of optical weak lensing. H_0 measurements will improve with increasing numbers of Cepheid or TRGB distances to supernova host galaxies, improving *Gaia* parallaxes of Galactic Cepheids, increasing numbers of strong gravitational-lens time delays, and continued attention to the systematic uncertainties in each method. Improving measurements of the CMB damping tail from ground-based experiments will provide increasingly strong constraints on solutions involving pre-recombination physics.

After beginning operations in early 2020, the DESI galaxy redshift survey will quickly exceed the size of the existing SDSS and BOSS surveys, enabling high precision BAO measurements of expansion history at $z \approx 0.7$–1.4 and, for the first time, percent-level measurements of structure growth through RSD. Precise BAO and RSD measurements at higher redshifts will come from DESI Lyman-α forest maps and the HETDEX and Subaru PFS galaxy surveys. The BAO measurements will complement increasingly precise measurements of the relative distance scale at $z < 1$ from the DES photometric supernova sample and from improved local supernova samples ($z < 0.1$) that provide a low-redshift anchor. Large galaxy samples will also enable more powerful applications of the Alcock-Paczynski effect, which can amplify the power of BAO and supernova distance measurements by converting them to constraints on the expansion rate $H(z)$.

The early-to-mid 2020s will see another major leap in observational capabilities with the advent of LSST, *Euclid*, and *WFIRST*. LSST will be the ultimate ground-based optical weak-lensing experiment, measuring several billion galaxy shapes over 20,000 deg^2 of the southern hemisphere sky, and it will detect and monitor many thousands of SNe per year. *Euclid* and *WFIRST* also have weak lensing as a primary science goal, taking advantage of the high angular resolution and extremely stable image quality achievable from space. Both missions plan large spectroscopic galaxy surveys, which will provide better sampling at high redshifts than DESI or PFS because of the lower infrared sky background above the atmosphere. *WFIRST* is also designed to carry out what should be the ultimate supernova cosmology experiment, with deep, high resolution, near-IR observations and the stable calibration achievable with a space platform. The 2020s will also see dramatic advances in CMB lensing from the Simons Observatory and, potentially, CMB-S4 and/or a space-based probe; cross-correlation with galaxy surveys allows precise tomographic measurements of clustering as a function of redshift.

If the anomalies suggested in Fig. 28.3 are real, then the experiments of the 2020s will map out their redshift, scale, and environment dependence in great detail, providing detailed empirical constraints on dynamical dark energy or modified gravity models. If these tensions dissipate with improved measurements, then the experiments of the 2020s will achieve much more stringent tests of the ΛCDM paradigm, with the potential to reveal deviations that are within the statistical uncertainties of current data. The critical clue to the origin of cosmic acceleration could also come from a surprising direction, such as laboratory or solar-system tests that challenge GR, time variation of fundamental "constants," or anomalous behavior of gravity in some astronomical environments. Experimental advances along these multiple axes could confirm today's relatively simple, but frustratingly incomplete, "standard model" of cosmology, or they could force yet another radical revision in our understanding of energy, or gravity, or the spacetime structure of the Universe.

References

[1] A. Einstein, Sitzungsber. Preuss. Akad. Wiss. Berlin (Math. Phys.), 142 (1917).

[2] Ya. B. Zel'dovich, A. Krasinski and Ya. B. Zeldovich, Sov. Phys. Usp. **11**, 381 (1968), [Gen. Rel. Grav.40,1557(2008); Usp. Fiz. Nauk95,209(1968)].

[3] A. Friedman, Z. Phys. **10**, 377 (1922), [Gen. Rel. Grav.31,1991(1999)].

[4] G. Lemaître, Annales de la Societe Scietifique de Bruxelles **47**, 49 (1927).

[5] E. Hubble, Proc. Nat. Acad. Sci. **15**, 168 (1929).

[6] A. Einstein and W. de Sitter, Proc. Nat. Acad. Sci. **18**, 213 (1932).

[7] For background and definitions, see Big-Bang Cosmology – Sec. 22 of this *Review*.

[8] A. G. Riess *et al.* (Supernova Search Team), Astron. J. **116**, 1009 (1998), [arXiv:astro-ph/9805201].

[9] S. Perlmutter *et al.* (Supernova Cosmology Project), Astrophys. J. **517**, 565 (1999), [arXiv:astro-ph/9812133].

[10] P. de Bernardis *et al.* (Boomerang), Nature **404**, 955 (2000), [arXiv:astro-ph/0004404].

[11] S. Hanany *et al.*, Astrophys. J. **545**, L5 (2000), [arXiv:astro-ph/0005123].

[12] D. H. Weinberg *et al.*, Phys. Rept. **530**, 87 (2013), [arXiv:1201.2434].

[13] C. Wetterich, Nucl. Phys. **B302**, 668 (1988), [arXiv:1711.03844].

[14] A. Joyce *et al.*, Phys. Rept. **568**, 1 (2015), [arXiv:1407.0059].

[15] S. M. Carroll *et al.*, Phys. Rev. **D70**, 043528 (2004), [arXiv:astro-ph/0306438].

[16] G. R. Dvali, G. Gabadadze and M. Porrati, Phys. Lett. **B485**, 208 (2000), [hep-th/0005016].

[17] C.M. Will, Living Reviews in Relativity, **9**, 3 (2006). See also the chapter on Experimental Tests of Gravitational Theory — in this *Review*.

[18] J. Wang, L. Hui and J. Khoury, Phys. Rev. Lett. **109**, 241301 (2012), [arXiv:1208.4612].

[19] M. Fairbairn and A. Goobar, Phys. Lett. **B642**, 432 (2006), [arXiv:astro-ph/0511029]; Y.-S. Song, I. Sawicki and W. Hu, Phys. Rev. **D75**, 064003 (2007), [arXiv:astro-ph/0606286]; C. Blake *et al.*, Mon. Not. Roy. Astron. Soc. **415**, 2876 (2011), [arXiv:1104.2948].

[20] T. Baker *et al.*, Phys. Rev. Lett. **119**, 25, 251301 (2017), [arXiv:1710.06394].

[21] E. V. Linder, Phys. Rev. **D72**, 043529 (2005), [arXiv:astro-ph/0507263].

[22] This is essentially the FoM proposed in the Dark Energy Task Force (DETF) report, A. Albrecht *et al.*, `astro-ph/0609591,`though they based their FoM on the area of the 95 in the $w_0 - w_a$ plane.

[23] For high accuracy, the impact of acoustic oscillations must be computed with a full Boltzmann code, but the simple integral for r_s captures the essential physics and the scaling with cosmological parameters.

[24] R. A. Sunyaev and Ya. B. Zeldovich, Astrophys. Space Sci. **7**, 3 (1970).

[25] D. Weinberg *et al.* (2013), [arXiv:1309.5380].

[26] C. Alcock and B. Paczynski, Nature **281**, 358 (1979).

[27] T. M. C. Abbott *et al.* (DES), Phys. Rev. **D98**, 4, 043526 (2018), [arXiv:1708.01530].

[28] T. M. C. Abbott *et al.* (DES), Astrophys. J. **872**, 2, L30 (2019), [arXiv:1811.02374].

[29] C. Hikage *et al.* (HSC), Publ. Astron. Soc. Jap. **71**, 2, Publications of the Astronomical Society of Japan, Volume 71, Issue 2, April 2019, 43, https://doi.org/10.1093/pasj/psz010 (2019), [arXiv:1809.09148].

[30] T. Hamana *et al.* (2019), [arXiv:1906.06041].

[31] B. Jain *et al.* (2015), [arXiv:1501.07897].

[32] W. L. Freedman *et al.* (HST), Astrophys. J. **553**, 47 (2001), [arXiv:astro-ph/0012376].

[33] N. Aghanim *et al.* (Planck) (2018), [arXiv:1807.06209].

[34] M. Betoule *et al.*, Astron. & Astrophys. **568**, 22 (2014).

[35] M. Sullivan *et al.* (SNLS), Astrophys. J. **737**, 102 (2011), [arXiv:1104.1444].
[36] N. Suzuki *et al.* (Supernova Cosmology Project), Astrophys. J. **746**, 85 (2012), [arXiv:1105.3470].
[37] D. M. Scolnic *et al.*, Astrophys. J. **859**, 2, 101 (2018), [arXiv:1710.00845].
[38] S. Alam *et al.* (BOSS), Mon. Not. Roy. Astron. Soc. **470**, 3, 2617 (2017), [arXiv:1607.03155].
[39] F. Beutler *et al.*, Mon. Not. Roy. Astron. Soc. **416**, 3017 (2011), [arXiv:1106.3366].
[40] A. J. Ross *et al.*, Mon. Not. Roy. Astron. Soc. **449**, 1, 835 (2015), [arXiv:1409.3242].
[41] M. Ata *et al.*, Mon. Not. Roy. Astron. Soc. **473**, 4, 4773 (2018), [arXiv:1705.06373].
[42] M. Blomqvist *et al.*, Astron. Astrophys. **629**, A86 (2019), [arXiv:1904.03430].
[43] Planck Collab. 2015 Results XIV, Astron. & Astrophys. **594**, A14 (2016).
[44] E. Aubourg *et al.*, Phys. Rev. **D92**, 12, 123516 (2015), [arXiv:1411.1074].
[45] E. Macaulay *et al.* (DES), Mon. Not. Roy. Astron. Soc. **486**, 2, 2184 (2019), [arXiv:1811.02376].
[46] A. G. Riess *et al.*, Astrophys. J. **876**, 1, 85 (2019), [arXiv:1903.07603].
[47] W.L. Friedman, Astron. J. **882** (2019) 34.
[48] K. C. Wong *et al.* (2019), [arXiv:1907.04869].
[49] V. Poulin *et al.*, Phys. Rev. Lett. **122**, 22, 221301 (2019), [arXiv:1811.04083].
[50] M. J. Jee *et al.*, Astrophys. J. **824**, 2, 77 (2016), [arXiv:1510.03962].
[51] H. Hildebrandt *et al.*, Mon. Not. Roy. Astron. Soc. **465**, 1454 (2017), [arXiv:1606.05338].
[52] M. A. Troxel *et al.* (DES), Phys. Rev. **D98**, 4, 043528 (2018), [arXiv:1708.01538].
[53] R. Mandelbaum *et al.*, Mon. Not. Roy. Astron. Soc. **432**, 1544 (2013), [arXiv:1207.1120].
[54] S. Singh *et al.*, Mon. Not. Roy. Astron. Soc. **491**, 1, 51 (2020), [arXiv:1811.06499].
[55] B. D. Wibking *et al.*, Mon. Not. Roy. Astron. Soc. **492**, 2, 2872 (2020), [arXiv:1907.06293].
[56] A. Leauthaud *et al.*, Mon. Not. Roy. Astron. Soc. **467**, 3, 3024 (2017), [arXiv:1611.08606].
[57] J. U. Lange *et al.*, Mon. Not. Roy. Astron. Soc. **488**, 4, 5771 (2019), [arXiv:1906.08680].
[58] S. Joudaki *et al.*, Mon. Not. Roy. Astron. Soc. **474**, 4, 4894 (2018), [arXiv:1707.06627].
[59] E. van Uitert *et al.*, Mon. Not. Roy. Astron. Soc. **476**, 4, 4662 (2018), [arXiv:1706.05004].
[60] N. Aghanim *et al.* (Planck) (2018), [arXiv:1807.06210].